Progress in Natural Science: Materials International 36 (2026) 131–142

HOSTED BY

Contents lists available at ScienceDirect

Progress in Natural Science: Materials International

journal homepage: www.elsevier.com/locate/pnsmi

Investigating the hot deformation behavior of Ti6Al4V alloys produced by powder metallurgy and forging

Yu Pan[a,*], Xinjing Wang[a], Guanghao Shi[b], Jianbo Tong[c], Jinshan Zhang[a], Xin Lu[a,**]

[a] Institute of Engineering Technology, National Engineering Research Center for Advanced Rolling and Intelligent Manufacturing, University of Science and Technology Beijing, Beijing, 100083, China
[b] China Aerospace Science and Technology Hunan Power Machinery Research Institute, Zhuzhou, 412002, China
[c] Key Laboratory of Advanced Titanium Alloys, AECC Beijing Institute of Aeronautical Materials, Beijing, 100095, China

ARTICLE INFO

Keywords:
Powder metallurgy
Forged metallurgy
DRX
Hot workability
Microstructural evolution

ABSTRACT

Powder metallurgy (PM), as an advanced manufacturing method, offers different microstructures and mechanical properties for titanium (Ti) alloys compared to forging metallurgy (FM). Therefore, investigating the hot deformation behaviour of PM and FM Ti alloys is of great significance. Herein, we systematically study the hot workability and hot deformed microstructure of PM and FM Ti6Al4V alloys deformed at 1000 °C–1200 °C and 0.01 s^{-1}~10 s^{-1} strain rates, so as to compare the different hot working properties. The true stress-strain curves were drawn through the isothermal compression tests, and the constitutive equations as well as hot processing maps of PM and FM alloys were further constructed. Results show that the PM alloy displays smaller hot deformation resistance, larger hot working safe zone and smaller instable zone when compared with FM alloy. PM alloy has higher dynamic recrystallization (DRX) degree. In DRX process, the PM alloy was dominated by discontinuous dynamic recrystallization (DDRX), while the FM alloy was dominated by continuous dynamic recrystallization (CDRX). This work reveals the difference between PM and FM Ti6Al4V alloys in hot deformation behavior and hot working properties, and further explains the underlying deformation mechanism.

1. Introduction

Titanium (Ti) and its alloys are widely used in aerospace, biomaterials, and marine fields due to their excellent strength, high-temperature resistance, corrosion resistance, and biocompatibility [1–3]. Since its inception, the Ti industry has focused on improving the manufacturing technology to optimize part quality and reduce production costs. FM technology is the main preparation method for Ti alloys [4,5]. However, the fabrication of Ti alloys by FM technology is challenging due to their complicated process and uneven microstructure, which seriously limits the cost and mechanical properties of FM parts. PM technology has the advantages of near-net-shape attributes, high material utilization levels, and chemically homogeneous microstructures, which provides an attractive method for manufacturing Ti alloys [6–10].

Unfortunately, defects such as insufficient density and coarse grain seriously affect the ductility and toughness of PM alloys, which seriously restricts the application of PM alloys. Therefore, it is necessary to develop subsequent processes to eliminate the sintering defects and further improve the material properties. The secondary hot deformation is an efficient method to optimize the microstructure of PM alloys. The pores in the microstructure are closed and the coarse grains are broken into fine grains after hot deformation [11–13]. DRX and dynamic recovery (DRV) are important mechanisms leading to grain refinement [14–16]. The kinetic constitutive analysis reflects the quantitative relationship between flow stress and thermodynamic parameters, and can directly describe the hot deformation behavior of materials [17]. The hot processing map can be used to optimize their machining process and machinability [18]. This tool plays a crucial role in exploring the high-temperature deformation mechanisms of Ti alloys. Zhao QY et al. [19] found that the dynamic α precipitation mechanism of ingot metallurgy (IM) Ti-5553 alloy is diffusion spheroidization and coarsening, and extensive DRX occurs at 900 °C–1050 °C. Chen XW et al. [20] identified the optimal hot working windows for the FM Ti-6Al-4V alloy in the α+β phase zone as the first domain (840–920 °C/0.01–0.049 s^{-1}) and the second domain (940–980 °C/0.11–1.65 s^{-1}). Park NK et al. [21]

* Corresponding author.
** Corresponding author.
E-mail addresses: panyu@ustb.edu.cn (Y. Pan), luxin@ustb.edu.cn (X. Lu).

https://doi.org/10.1016/j.pnsc.2025.12.006
Received 2 September 2025; Received in revised form 11 December 2025; Accepted 14 December 2025
Available online 27 December 2025

employed the dynamic materials model (DMM) to confirm that the dominant deformation mechanism of the FM Ti-6Al-4V alloy in the α+β phase region is DRV, while the unstable deformation is attributed to the flow localization and dynamic grain growth of the transformed β phase, respectively. However, most of the current researches focus on the hot deformation characteristics of traditional FM Ti alloys [22–24]. Comparatively, PM Ti alloys possess more uniform and finer microstructure when deformed in the β single-phase zone due to the stable microstructure obtained through high-temperature sintering [25,26], which may change the deformation processing window. Therefore, it is of great significance to explore the hot deformation behavior and microstructural evolution of PM Ti alloys in the β single-phase zone. Comprehensive comparison of deformation mechanism differences between PM and FM Ti alloys, and establishing the optimal processing windows for PM Ti alloys is essential for practical engineering applications.

In this paper, the hot deformation behaviors of PM and FM Ti6Al4V alloys were systematically investigated, and the differences in hot processing maps and hot working properties were determined by analysing microstructural evolution. This work reveals the differences and underlying mechanisms of the hot deformation behaviors between PM and FM Ti6Al4V alloys.

2. Experimental procedures

The PM alloy was produced by pressureless sintering route. The raw materials were hydride-dehydride (HDH) Ti6Al4V powders (D_{50} = 27.67 μm, 0.20 wt% O) supplied by the Tian Tai Long Metal Materials Co., Ltd. China. The commercially available FM alloy is supplied by the Dongguan Huijing Metal Materials Co., Ltd. China. The preparation of PM alloy mainly includes two parts: Firstly, the raw powders were compacted by cold isostatic pressing at 250 MPa with silicone envelope for 1 min. Secondly, the samples were sintered in a tube furnace under the protection of high-purity argon atmosphere (99.999 % purity) with the heating rate of 5 °C/min to 1000 °C and 2 °C/min to 1300 °C. After holding at 1300 °C for 2 h, it began to cool to 800 °C at a rate of 5 °C/min. Finally, the PM alloy was obtained after cooling to room temperature. Table 1 shows the specific chemical compositions of PM and FM alloys. In addition, some samples cut from PM and FM alloys were heated to 1100 °C, then immediately water-quenched.

The samples used in isothermal compression tests are cut from the middle area of PM and FM alloys, and then machined into smooth surfaces with electric spark cutting to φ8 × 12 mm. The isothermal compression tests were carried out on the Gleeble-3500 thermal testing machine. Considering the β-transus temperature of Ti6Al4V alloy and practical hot-working temperature ranges of PM alloys [27,28], the testing temperatures were selected as 1000 °C, 1100 °C, and 1200 °C, the strain rates are 0.01 s^{-1}, 0.1 s^{-1}, 1 s^{-1}, and 10 s^{-1}, and the maximum deformation is 70 %. Before compression, the graphite foils and tantalum plates were coated between the end face of sample and extrusion head to increase conductivity. The samples were heated at 10 °C/s and held for 3 min. After isothermal compression testing, the samples were immediately water-quenched. Three samples were used for parallel experiments under each condition. The quenched samples after cooling were machined and analyzed along the compression direction.

The microstructures of deformed samples were observed using a confocal laser scanning microscope (OLS4100, Japan). The grain structure, DRX grain distribution, and grain boundary misorientation angle of the deformed samples were studied using electron backscatter diffraction (EBSD, FEI Quanta 450F, USA). The samples were electropolished at −20 °C and 25 V. The as-compressed microstructure was analyzed by transmission electron microscope (TEM, Tecnai G2 F20, USA). TEM foil samples of PM and FM alloys were fabricated by ion beam thinning.

Table 1
Chemical compositions of PM and FM Ti6Al4V alloys (wt.%).

Raw materials	Ti	O	Al	C	V	H	N
PM alloy	Bal.	0.27	6.01	0.027	4.08	0.018	0.023
FM alloy	Bal.	0.20	6.2	0.1	4.1	0.015	0.05

3. Results

3.1. Initial microstructures

Fig. 1 presents the initial microstructures of PM and FM alloys. The PM alloy shows a typical Widmanstätten structure (Fig. 1a–d). The α phase is presented along the grain boundaries, while the interior of the grains consists of elongated α plates and interlamellar β phase. The grain size is relatively coarse (G_{avg} = 31.3 μm), which conforms to the characteristics of PM alloy cooling slowly at high temperature. The inverse pole figure (IPF) in Fig. 1c displays the irregular grain morphologies and randomly distributed grain colors. The FM alloy displays a lamellar structure, and the grain boundary presents obvious irregular characteristics, as many plate-like β phases are distributed in the irregular α grains. The α grains are elongated in the forging process. In addition, a certain amount of equiaxed α grains are distributed around the deformed grains (Fig. 1e–f). The IPF image in Fig. 1g displays the relatively smaller grain size (G_{avg} = 4.98 μm) for FM alloy.

3.2. Stress-strain curves of high-temperature compression

Fig. 2 shows the true strain-stress curves of PM and FM alloys under different hot working parameters. The flow stress (σ) of PM and FM alloys both decreases with the increase of deformation temperature and the decrease of strain rate ($\dot{\varepsilon}$). During this process, the work hardening and dynamic softening jointly affect the flow behaviors of alloys [29, 30]. As shown in Fig. 2a–b and d-e, those curves initially rise with increasing strain at the beginning of compression for both PM and FM alloys. With the increase of strain, the flow stress drops to the steady-state value. For Fig. 2c and f, some curves initially rise and then fall with increasing strain. It is noteworthy that this phenomenon disappears in the FM alloy at the strain rates above 0.1 s^{-1}, whereas it persists in the PM alloy even at the strain rate of 10 s^{-1}. This suggests that the softening mechanism present in the PM alloy predominates over work hardening at high strain rates.

3.3. Kinetic analysis of hot deformation process

The deformation activation energy Q directly reflects the hot deformation resistance of materials [31,32]. The value of Q can be expressed as shown below:

$$\dot{\varepsilon} = A\left[\sin h(\alpha\sigma)^n \exp\left(-\frac{Q}{RT}\right)\right. \quad (1)$$

where A, n and α are the constants, T is the temperature (K), R is the gas constant (8.314 J mol^{-1} K^{-1}). Under the condition of hot deformation, the constitutive equation can also be expressed by exponential equation and power function:

$$\dot{\varepsilon} = B_1\sigma^n \quad (2)$$

$$\dot{\varepsilon} = B_2 \exp(\beta\sigma) \quad (3)$$

Taking the logarithm of equations (2) and (3):

$$\ln \dot{\varepsilon} = \ln B_1 + n_1 \ln(\sigma) \quad (4)$$

$$\ln \dot{\varepsilon} = \ln B_2 + \beta\sigma \quad (5)$$

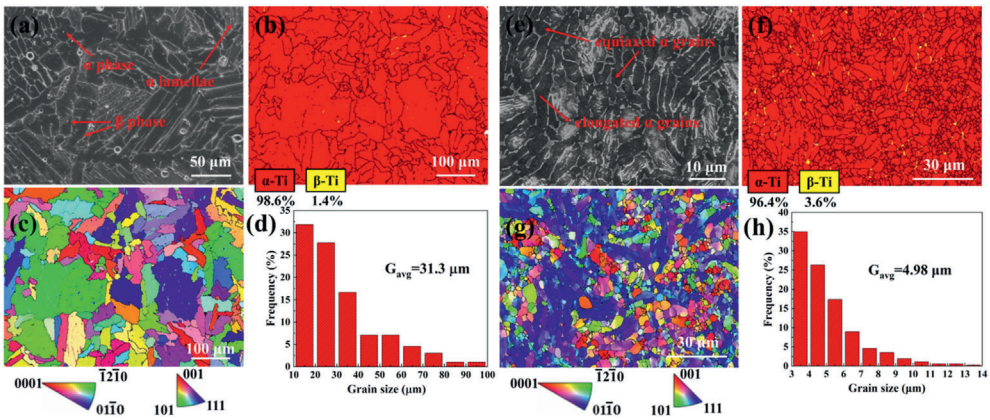

Fig. 1. The microstructure of the PM (a–d) and FM (e–h) alloys: (a) (e) SEM image; (b) (f) Phase fraction of α phase and β phase; (c) (g) IPF map; (d) (h) Grain size distibution.

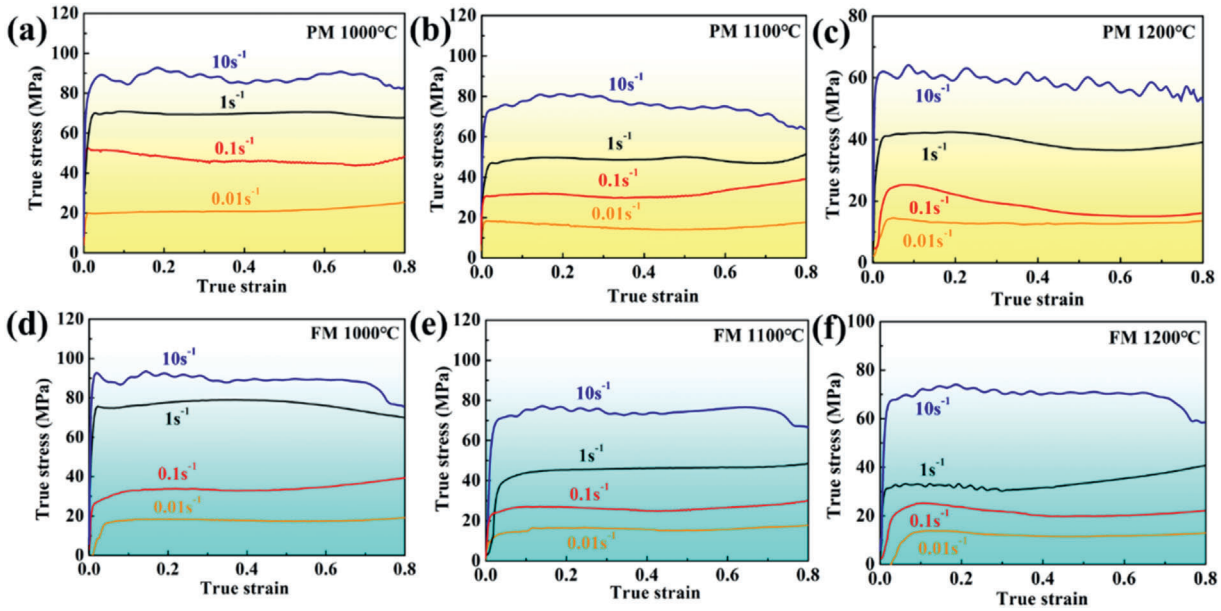

Fig. 2. True stress-strain curves of Ti6Al4V alloys. PM alloy: (a) 1000 °C; (b) 1100 °C; (c) 1200 °C; FM alloy: (d) 1000 °C; (e) 1100 °C; (f) 1200 °C.

where α = β/ n_1, B_1 and B_2 are constants. By linear fitting the peak stresses and corresponding strain rates of PM and FM alloys, the relation curves of σ-ln ($\dot{\varepsilon}$) and ln(σ)-ln ($\dot{\varepsilon}$) are shown in Fig. 3. Both materials are suitable for solving the constitutive equation by least squares linear regression. According to equations (4) and (5), the slopes of two curves are n_1 and β, respectively. It can be calculated from Fig. 3a–b that the average values of β and n_1 are 0.213 and 9.440. From Fig. 3c–d, the values of β and n_1 of FM alloy are calculated to be 0.233 and 9.615. Thus, the α values of PM and FM alloy are determined as 0.022 and 0.024, respectively.

The Q value can be expressed from equation (1), as shown below:

$$Q = R \cdot \frac{\partial \ln \dot{\varepsilon}}{\partial \ln(\sin h(\alpha\sigma))} \cdot \frac{\partial \ln(\sin h(\alpha\sigma))}{\partial \ln(1/T)} = R \cdot n \cdot n_2 \tag{6}$$

The relation curves of $ln(sinh(\alpha\sigma))$-1000/T and ln ($\dot{\varepsilon}$)-$ln(sinh(\alpha\sigma))$ are shown in Fig. 4. The slopes of two curves are n and n_2/1000, respectively. From Fig. 4a–b, the average values of n and n_2/1000 of PM alloy are 4.02 and 3.16, respectively. By linear fitting to Fig. 4c–d, the average values of n and n_2/1000 of FM alloy are 4.22 and 3.55, respectively. Thus, the Q values of PM and FM alloys are 105.61 kJ mol^{-1} and 124.55 kJ mol^{-1}, respectively.

From equation (1), the A values can be obtained according to the Q, R, T, and n, as shown in Table 2. The relationship between temperature and A value was fitted as a power function (Fig. 5). Finally, the constitutive equations of PM and FM alloys can be presented as:

$$\text{PM alloy: } \dot{\varepsilon} = A\left[\sin h(0.02\sigma)^{3.45} \exp\left(-\frac{1.2\times10^5}{RT}\right)\right], \quad A = 4.9 \times 10^{-17} \exp\left(-\frac{T}{25.25}\right) + 5.5 \times 10^4$$

$$\text{FM alloy: } \dot{\varepsilon} = A\left[\sin h(0.02\sigma)^{3.16} \exp\left(-\frac{2.5\times10^5}{RT}\right)\right], \quad A = 5.5 \times 10^{-5} \exp\left(-\frac{T}{26.22}\right) - 6.5 \times 10^{11}$$

3.4. Hot processing map

In the DMM, the input external force P in the deformation process mainly has two parts [33,34]:

$$P = \sigma\dot{\varepsilon} = G + J = \int_0^{\dot{\varepsilon}} \sigma d\dot{\varepsilon} + \int_0^{\sigma} \dot{\varepsilon} d\sigma \tag{7}$$

where G and J represent the power dissipation of energy in the form of heat and microstructure change, respectively. The use of power dissipation coefficient in hot processing can define the energy utilization rate

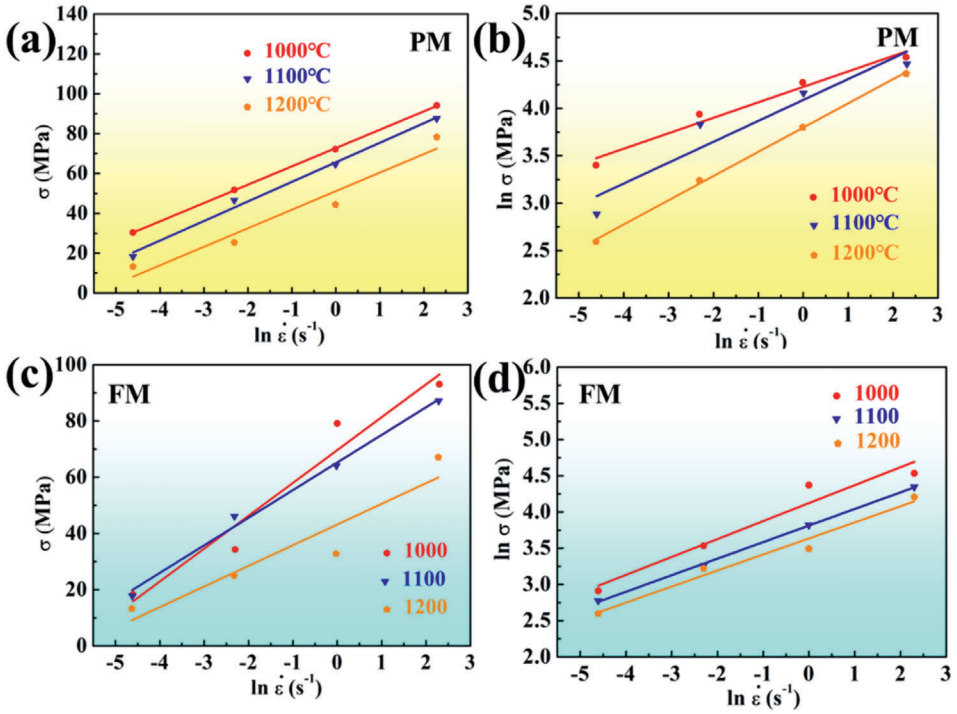

Fig. 3. Relationships between the stable flow stress and strain rate. PM alloy: (a) σ-ln ($\dot{\varepsilon}$); (b) ln(σ)-ln ($\dot{\varepsilon}$); FM alloy: (c) σ-ln ($\dot{\varepsilon}$); (d) ln(σ)-ln ($\dot{\varepsilon}$).

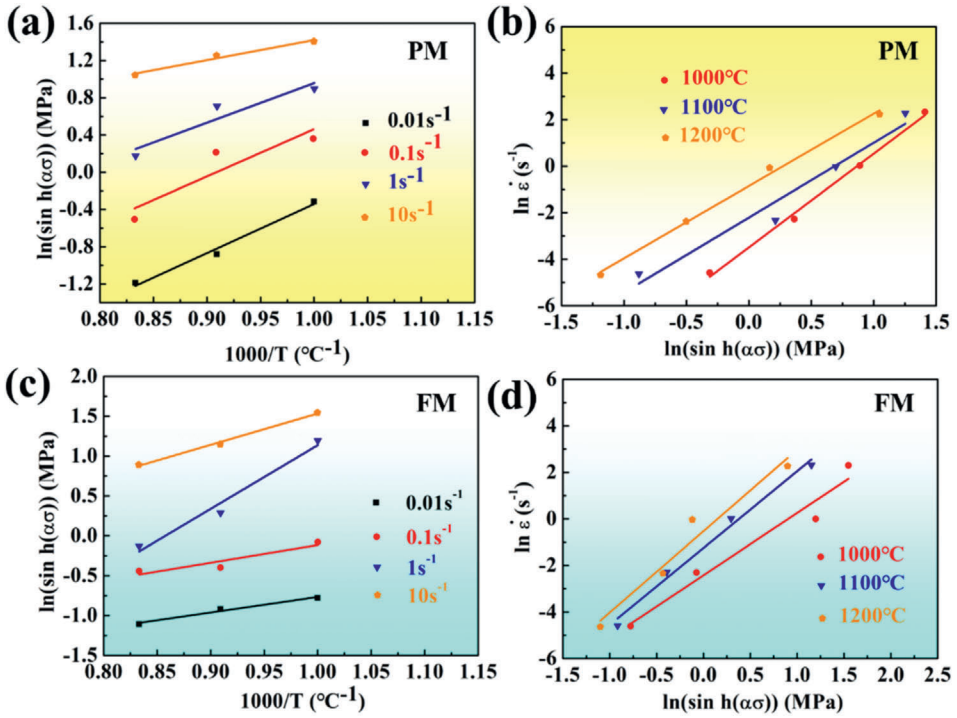

Fig. 4. Relationships between the stable flow stress and variations of strain rate and temperature. PM alloy: (a) $ln(sinh(\alpha\sigma))$-1000/T; (b) ln ($\dot{\varepsilon}$)-$ln(sinh(\alpha\sigma))$; FM alloy: (c) $ln(sinh(\alpha\sigma))$-1000/T; (d) ln ($\dot{\varepsilon}$)-$ln(sinh(\alpha\sigma))$.

Table 2
A values of the two alloys at different temperatures.

Temperature/°C	PM alloy	FM alloy
1000	5.55×10^4	1.37×10^{12}
1100	5.59×10^4	9.11×10^{13}
1200	7.69×10^4	4.16×10^{15}

of materials, defined as η, as shown below:

$$\eta = \frac{J}{J_{max}} = \frac{2m}{1+m} \tag{8}$$

where m is strain rate sensitive index, which can be expressed by equation (9):

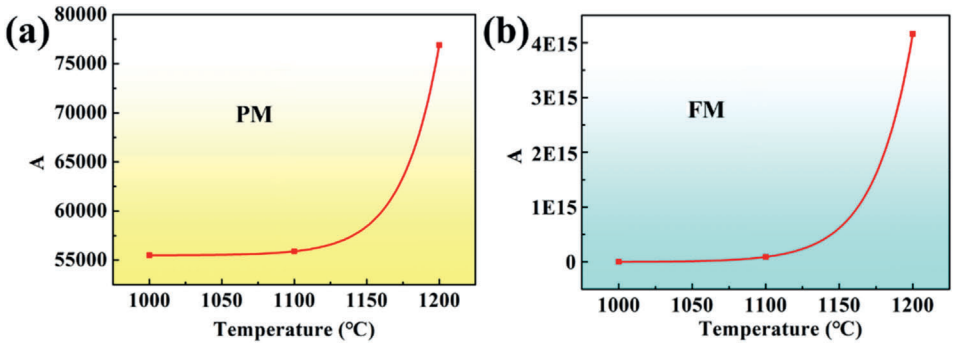

Fig. 5. Relationships between the A values and temperatures for (a) PM and (b) FM alloys.

$$m = \frac{\partial J}{\partial G} = \frac{\dot{\varepsilon}\partial\sigma}{\sigma\partial\dot{\varepsilon}} = \frac{\partial(\ln\sigma)}{\partial(\ln\dot{\varepsilon})} \tag{9}$$

Prasad Y.V.R.K et al. [35,36] proposed the condition of material plastic deformation instability:

$$\xi(\dot{\varepsilon}) = \frac{\partial \ln\left(\frac{m}{m+1}\right)}{\partial \ln \dot{\varepsilon}} + m < 0 \tag{10}$$

Therefore, the hot processing maps of PM and FM alloys are constructed, as shown in Fig. 6a–b, respectively. According to Ref. [37], the region that η values are greater than 0.4 is considered to be the reasonable hot working window. Thus, the PM alloy has larger safe processing window than that of FM alloy (Fig. 6). By comparison, the optimal zone (η ≥ 0.4) for PM alloy is the 1025 °C–1200 °C/0.01 s^{-1}~0.1 s^{-1} (Fig. 6a), while the optimal zone for FM alloy is only the 1000 °C–1050 °C/0.01 s^{-1}~0.56 s^{-1} (Fig. 6b). Additionally, the instable zone is showed as the shade region in Fig. 6. It is known that the PM alloy exhibits smaller instable zone when compared to FM alloy (1000 °C–1040 °C/1 s^{-1}~10 s^{-1} *vs.* 1000 °C–1070 °C/0.56 s^{-1}~10 s^{-1}). Additionally, Fig. 7 presents the hot processing maps at different strain levels, illustrating a clear trend of shrinking safe processing zones for both alloys as strain increases. In comparison, the PM alloy exhibits a larger safe zone and a relatively smaller instable zone than the FM alloy in Fig. 7a–f. This is also consistent with the observations in Fig. 6. It is noteworthy that the safe processing zone of the FM alloy gradually increases under high-temperature and low-strain-rate conditions, whereas that of the PM alloy decreases. This divergent behavior can be likely attributed to their distinct strain softening mechanisms.

Furthermore, the macroscopic morphologies of all specimens after compression testing are shown in Fig. 8. It is evident that cracking tends to occur under the condition of low temperature and high strain rate. Specifically, the FM alloys crack at the processing window of 1000–1100 °C and 1-10 s^{-1}, while the PM alloys crack at only 1000 °C and 1-10 s^{-1}. These observations are corresponding to the predictions of hot processing maps in Figs. 6 and 7. PM billets are typically precision-forged with a deformation strain of ≤50 % [38,39]. Therefore, the appropriate hot working parameters are determined as 1000–1150 °C/0.01–0.14 s^{-1} and 1150–1200 °C/0.14–10 s^{-1} for PM alloy. Comparatively, the FM alloy need the suitable parameters of 1000–1030 °C/0.01–0.37 s^{-1}, 1170–1200 °C/0.01–0.03 s^{-1} and 1170–1200 °C/2.7–10 s^{-1} under the same strain.

3.5. Microstructural evolution

Fig. 9 shows the deformed microstructure of PM and FM alloys in their respective instable and safe zones. For the PM alloy deformed at 1000 °C/10 s^{-1}, there are some unevenly deformed α precipitation bands in instable zone (Fig. 9a). It is worth noting that the shear bands (angle of 45° with the matrix) are observed for PM alloy (Fig. 9b). In addition, the acicular martensite α′ phase formed during the rapid cooling is also found. For the FM alloy deformed at 1000 °C/10 s^{-1}, coarse grains can be seen in Fig. 9e, indicating that the α grains are rapidly spheroidized and grow up in instable zone [40]. Furthermore, the combined effects of rapid deformation and cooling lead to the formation of numerous discontinuous β-phase particles, which even agglomerate into clusters (Fig. 9e and f). For the PM alloy deformed at 1100 °C/0.01 s^{-1}, there are many lathy β grains and fine α grains along the deformation direction (Fig. 9c and d). Compared with PM alloy, some DRV features are obviously shown in FM alloy deformed at 1100 °C/0.01 s^{-1}, such as irregular and serrated border β grains (Fig. 9g and h). Due to the high temperature and rapid cooling, acicular martensite α′ phase is found in the grain [41].

The deformation microstructure in the instable zone and safe zone are analyzed using EBSD. Fig. 10 shows the IPF maps and DRX distribution maps of PM and FM alloys deformed at 1000 °C/10 s^{-1} and 1100 °C/0.01 s^{-1}. According to the grain orientation spread (GOS) values, the microstructure can be divided into DRX grains, substructures and deformed grains, which are marked with blue, yellow, and red,

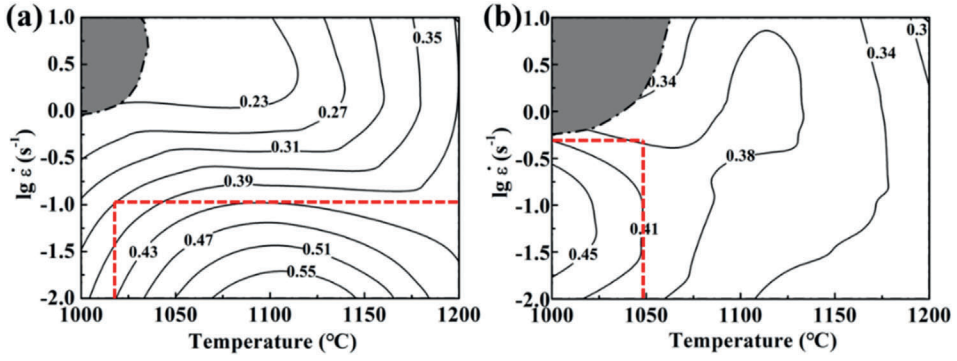

Fig. 6. The hot processing maps of PM (a) and FM (b) alloys at peak stress. The inner areas of the red dashed lines represent the safe zones and the grey-shaded regions represent the instable zones.

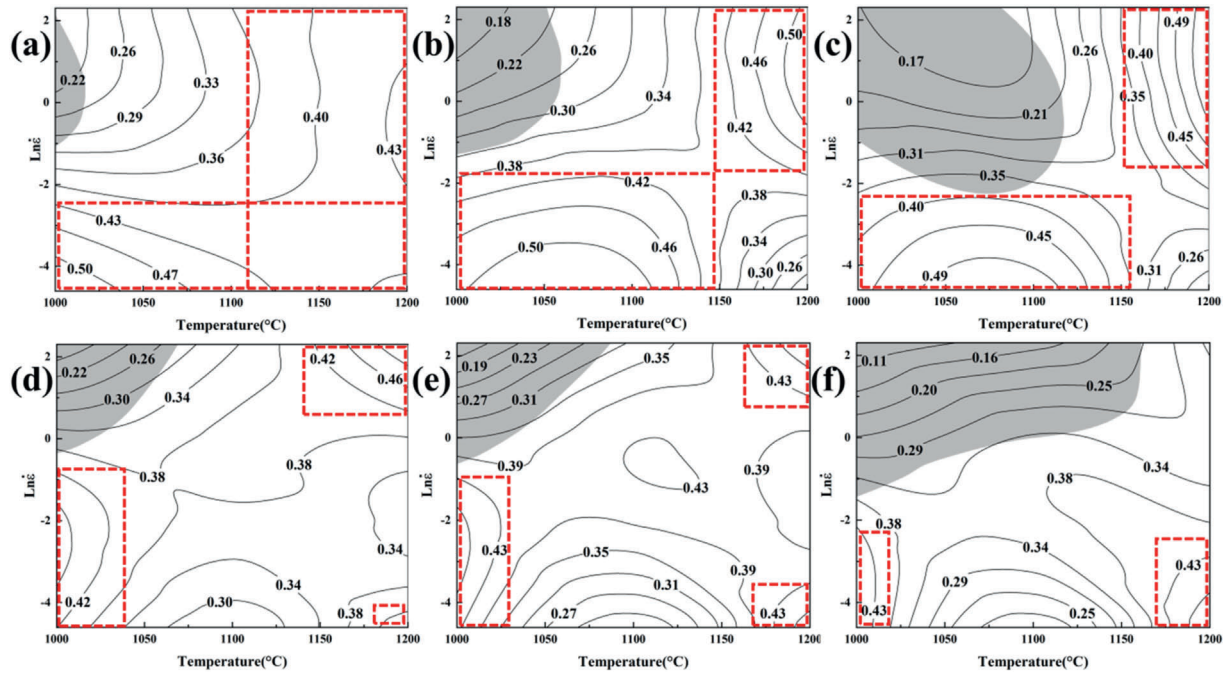

Fig. 7. The hot processing maps of PM (a–c) and FM (d–f) alloys. PM alloy: (a–c) ε = 0.2, 0.5, 0.8; FM alloy: (d–f) ε = 0.2, 0.5, 0.8. The inner areas of the red dashed lines represent the safe zones and the grey-shaded regions represent the instable zones.

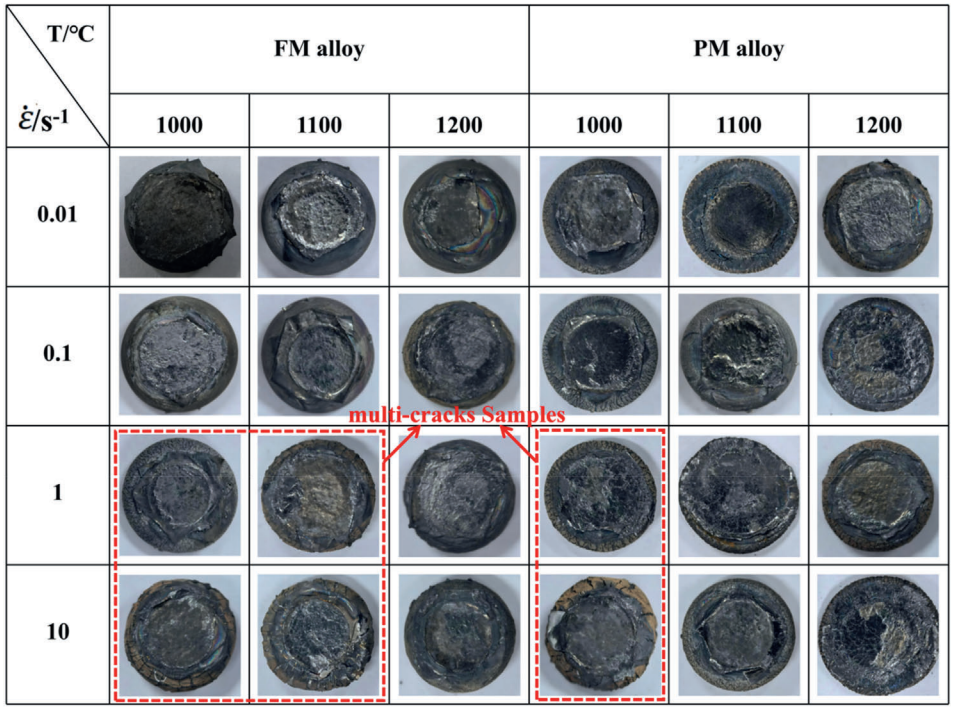

Fig. 8. Stereoscopic microscopic morphologies of the samples after hot compression testing.

respectively. As shown in Fig. 10a–b, the microstructure of PM alloy deformed at 1000 °C/10 s^{-1} is mainly composed of α lamellar (α_L) and few DRX grains. Compared with the safe zone, the decomposition of α_L and deformed grains are promoted by the low strain rate (Fig. 10c). From Fig. 10c–d, the PM alloy has a large number of fine DRX grains. In addition, the grain size is more uniform than that of FM alloy deformed at 1000 °C/10 s^{-1}. For FM alloy (Fig. 10e), the microstructure is mainly lamellar. From Fig. 10f, the proportion of deformed grains is relatively high while the DRX is low. For FM alloy deformed at 1100 °C/0.01 s^{-1}, the grain size is obviously coarsened (Fig. 10g), and the degree of DRX increases significantly compared with the instable zone. Moreover, the proportions of DRX grains and deformed grains for PM alloy (1000 °C/10 s^{-1}) are 13.5 % and 11.9 % (Fig. 10b), respectively. For comparison, the respective proportions of FM alloy (1000 °C/10 s^{-1}) are 9.3 % and 33.0 % (Fig. 10f). For the PM alloy deformed at 1100 °C/0.01 s^{-1}, the proportion of DRX grains is 24.2 % (Fig. 10d). However, the proportion of DRX microstructure for FM alloy (1100 °C/0.01 s^{-1}) is relatively small, at only 15.02 % (Fig. 10h).

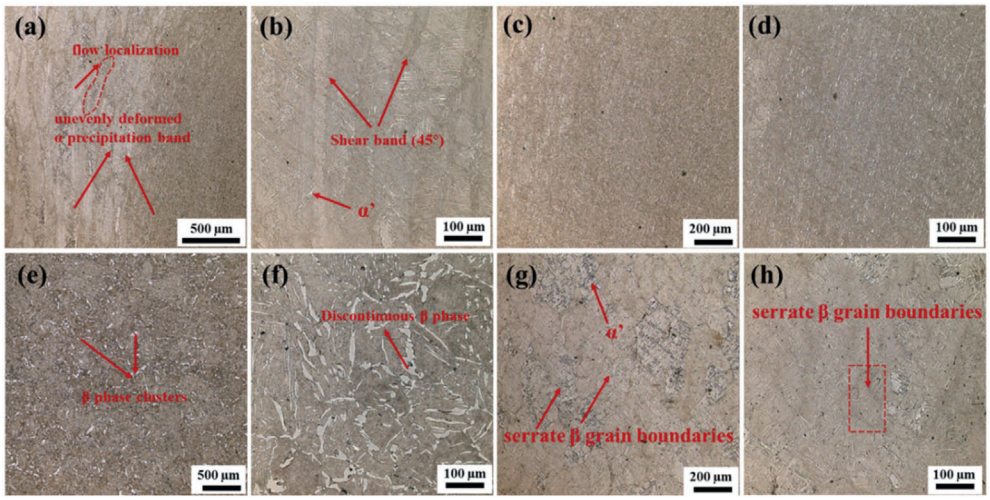

Fig. 9. OM images of the PM and FM alloys. PM alloy: (a) 1000 °C/10 s^{-1}; (b) Magnified image of (a); (c) 1100 °C/0.01 s^{-1}; (d) Magnified image of (c); FM alloy: (e) 1000 °C/10 s^{-1}; (f) Magnified image of (e); (g) 1100 °C/0.01 s^{-1}; (h) Magnified image of (g).

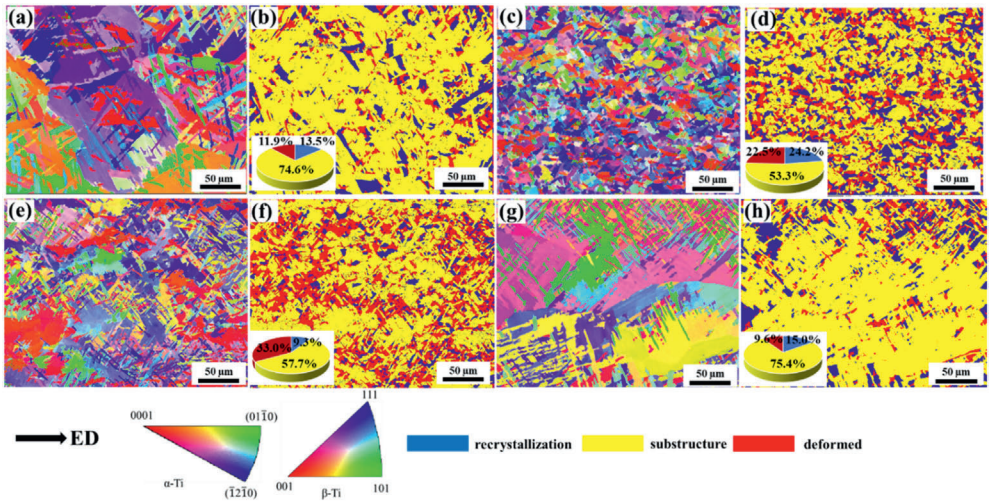

Fig. 10. IPF maps and DRX maps of the PM and FM alloys. PM alloy: (a), (b) 1000 °C/10 s^{-1}; (c), (d) 1100 °C/0.01 s^{-1}; FM alloy: (e), (f) 1000 °C/10 s^{-1}; (g), (h) 1100 °C/0.01 s^{-1}.

The dislocation density distributions for PM and FM alloys deformed at 1000 °C/10 s^{-1} are shown in Fig. 11. The local misorientation values in Kernel Average Misorientation (KAM) map are divided into low dislocation density (0–1), medium dislocation density (1–2) and high dislocation density (2–5). Comparing with the previous IPF maps (Fig. 10b and f), it is found that DRX is mainly prone to occur in the areas with low dislocation density. The dislocation density is relatively concentrated in the deformed structure of FM alloy (1000 °C/10 s^{-1}) when compared with PM alloy deformed at 1000 °C/10 s^{-1}. In addition, Fig. 12 studies the grain boundary information of PM and FM alloys deformed at 1100 °C/0.01 s^{-1}. Results show that the low angle grain boundary mainly exists in the deformed grains with incomplete DRX, resulting in the formation of subgrains [42]. For PM alloy, the orientation difference angle of the nuclei is significantly higher than that of FM alloy (87.1 % vs. 68.6 %), as shown in Fig. 12b and d. In addition, the PM alloy exhibits a more homogeneous distribution of grain boundary angles compared to the FM alloy.

The different DRX mechanisms of PM alloy (1100 °C/0.01 s^{-1}) and FM alloy (1100 °C/0.01 s^{-1}) are further observed by TEM. For PM alloy, there are obvious DRX grains appear at the junction of β grains (Fig. 13a), which are determined as α-Ti (Fig. 13a1). Subsequently, the growth of DRX grains (Fig. 13b) is caused by the migration and expansion of prominent HAGBs (Fig. 13c). Furthermore, dislocation plugging in the β matrix near HAGBs is significantly higher than that in DRX grains (Fig. 13c and d). Fig. 13f shows the well-grown DRX grain morphology, which has no internal dislocations. For FM alloy, DRX grains are formed inside β grains, and the grown DRX grains are surrounded by obvious HAGBs (Fig. 13e), which were transformed from vague LAGBs [43,44]. As shown in Fig. 13f, DRX grains are surrounded by a large number of dislocations and sub-grains. Meanwhile, there are many dislocations in DRX grains, but the dislocation density is significantly higher than that in DRX grains of PM alloy. These results indicate that the nucleation of DRX grains in FM alloys is due to the merger of subgrains, with the conversion of aggregated LAGBs to HAGBs. As the selected area electron diffraction (SAED) images shown in Fig. 13g1-g2, the bright phase (point 2) is hexagonally structured α-Ti, and the dark phase (Fig. 13g) is determined to be the β-Ti phase (point 3).

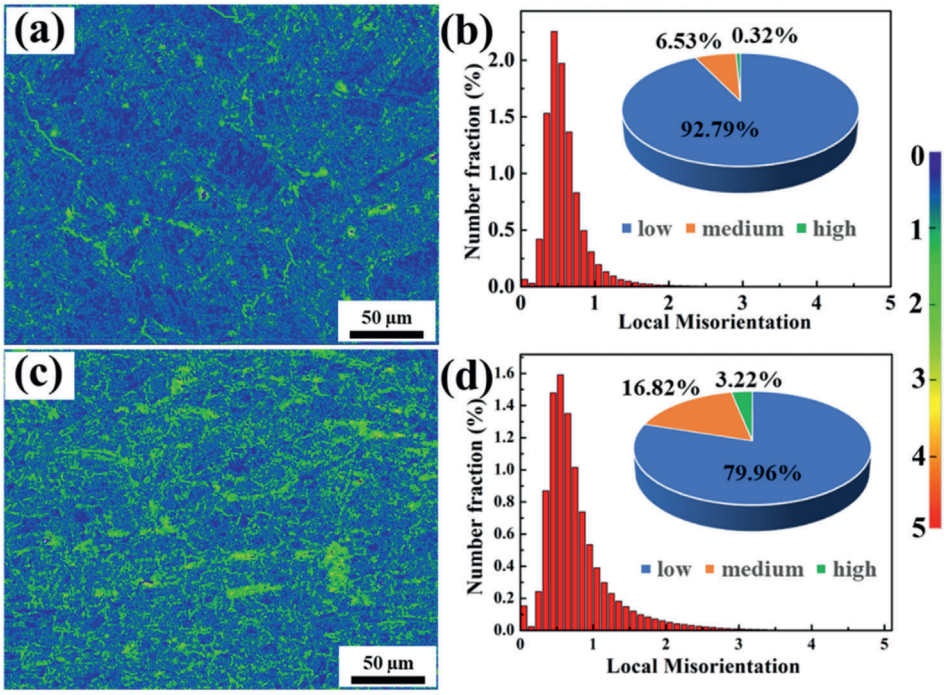

Fig. 11. KAM maps (a, c) and dislocation density distribution maps (b, d) of the PM (a, b) and FM (c, d) alloys deformed at 1000 °C/10 s^{-1}.

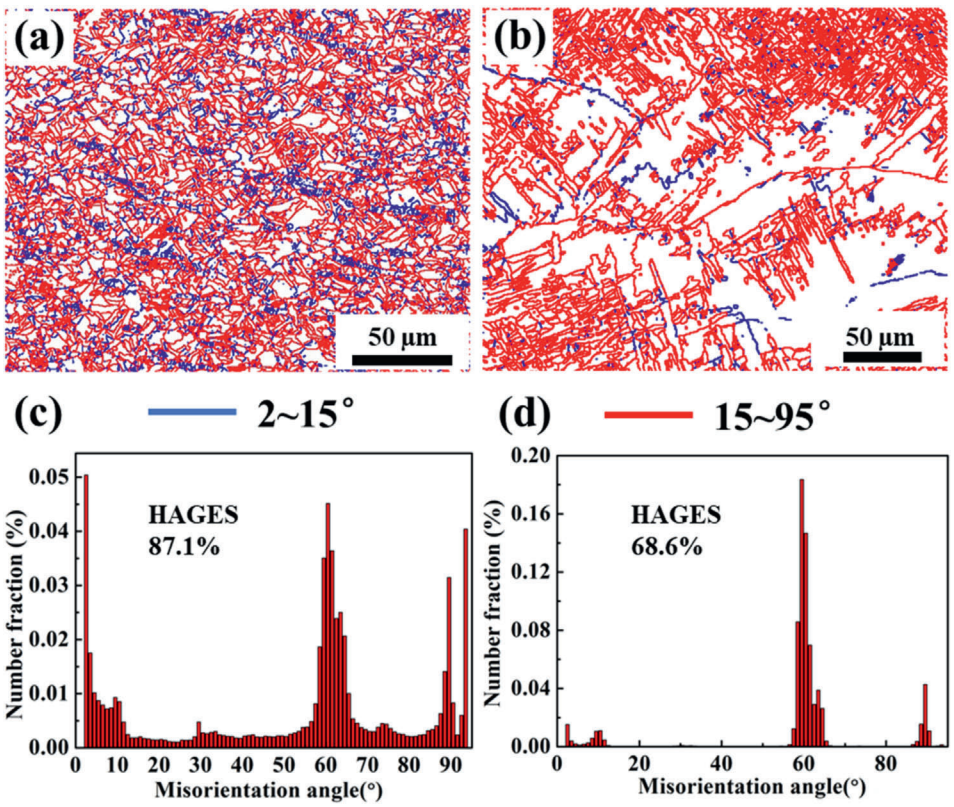

Fig. 12. Grain boundary misorientation angles (a, b) and distributions maps (c, d) of PM (a, c) and FM (b, d) alloys deformed at 1100 °C/0.01 s^{-1}.

4. Discussion

4.1. Deformation mechanisms

The DRX grains of PM alloy are mainly formed at the grain boundary with an equiaxed structure (Fig. 10c–d), while the DRX grains of FM alloy are mainly nucleated inside the grain boundary (Fig. 10g–h). It should be noted that the dislocation density in the DRX grain in FM alloy is higher than that of PM alloy (Fig. 11), indicating that the different DRX mechanism for the two alloys. To further compare the differences in

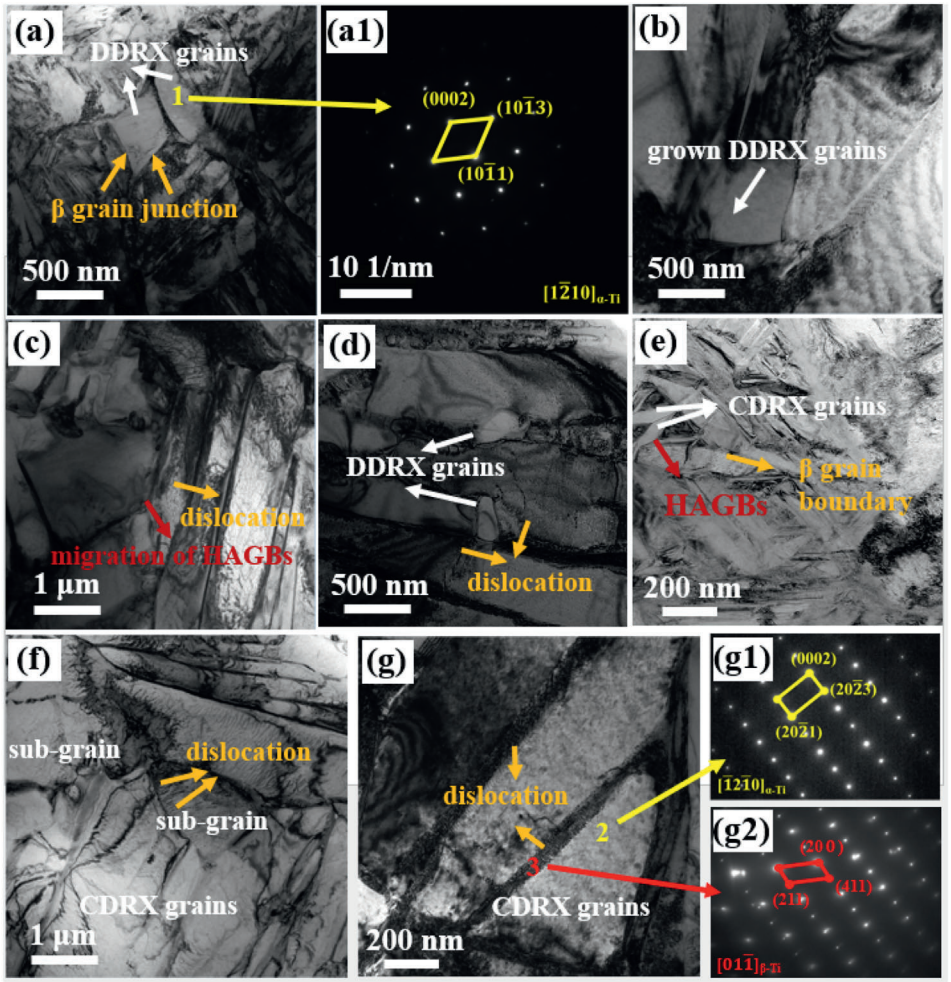

Fig. 13. TEM observations of PM (a–d) and FM (e–g) alloys. (a–d) bright field images; (a1) SAED pattern of point 1. (e–g) bright field images; (g1)-(g2) SAED pattern of points 2 and 3.

DRX mechanisms between the two alloys, Fig. 14 shows the variations of the misorientation angle (MA) calculated on the piecewise images in Fig. 10c and e. The MA of PM alloy are both below 4.0°. For FM alloy, the internal orientation of DRX grain changes significantly. At this time, HAGBs has not been fully formed [45–47], and the MA of FM alloy are greater than 8° and 9°, respectively. Therefore, the subcrystal rotation of

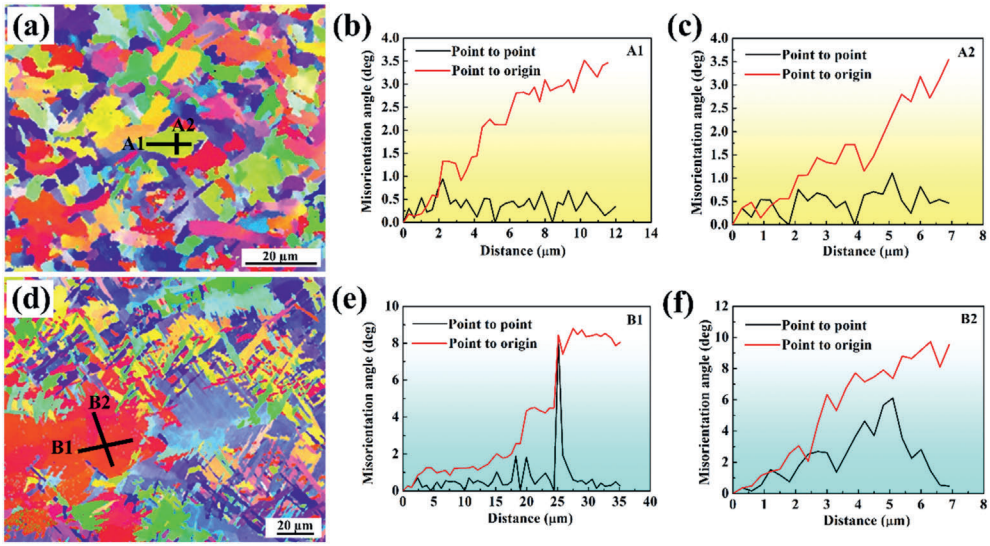

Fig. 14. Segment enlarged IPF maps and variations of MA values. (a) Segment enlarged IPF map of PM alloy; (b), (c) MA values along the arrows of A1 and A2, respectively; (d) Segment enlarged IPF map of FM alloy; (e), (f) MA values along the arrows of B1 and B2, respectively.

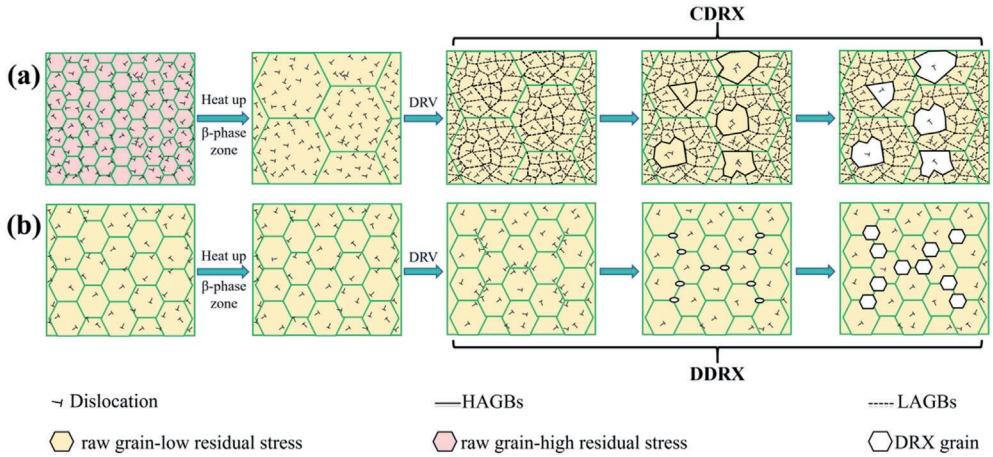

Fig. 15. Schematic diagram showing the hot-deformation mechanisms for (a) FM alloy and (b) PM alloy.

FM alloy plays an important role for the formation of DRX grains compared with PM alloy.

From the above analysis of Figs. 13 and 14, the DRX mechanism in PM alloys is DDRX. It can be inferred from Fig. 13 that the grain boundaries of the deformed grains provide nucleation locations for the DRX grains. The existence of deformation strain energy induces HAGBs to migrate [48]. During this migration, subgrains do not undergo significant rotation, while dislocations in the adjacent regions are continuously absorbed [49]. This is consistent with Fig. 7a–c, which show that the PM alloy has a larger safe zone that gradually decreases with increasing strain. The underlying reason is that the deformation process is dominated by DDRX, which rapidly generates strain-free equiaxed grains and causes a sharp drop in dislocation density, thereby leading to the rapid strain softening. However, it subsequently fails to provide sufficient driving force for continued recrystallization, resulting in poor sustainability of the softening effect. Different from that, the main DRX mechanism of FM alloy is CDRX. The slip and climb out of the dislocations along the LAGBs realize the transformation of LAGBs to the new HAGBs, resulting in smaller variations in dislocation density inside and outside the CDRX grain than the DDRX grain [50]. The sustained driving force provided by a high dislocation density for CDRX promotes the expansion of the safe zone at high temperatures and low strain rates with increasing strain (Fig. 7d–f). However, this occurs at the expense of softening efficiency, resulting in a significantly smaller safe zone. Fig. 15 presents the detailed schematic diagram illustrating the hot-deformation mechanisms for PM and FM alloys.

4.2. Stable and excellent microstructure of PM alloy

The pronounced difference in hot workability between the PM and FM alloys can be attributed to their distinct initial microstructures at high temperature. The microstructures of the two alloys after heating at 1100 °C are shown in Fig. 16a and b, respectively. The microstructure of PM alloy heated to 1100 °C is still Widmanstätten microstructure, and the grain size does not increase significantly (Fig. 16a). However, the thickness of α lamellae grows rapidly and the grains coarsen significantly when FM alloy is heated to 1100 °C (Fig. 16b). Compared with the high-temperature microstructures for the two alloys, PM alloy has a finer microstructure and higher grain boundary density. This is because that the PM alloy has already been sintered at 1300 °C, the as-sintered microstructure has a higher grain growth energy barrier than that of FM alloy. For PM alloy, the fine grain provides paths for the grains slipping along the boundaries easily, leading to the decrease of deformation resistance. In contrast, the large residual stress come from forging process induces the significant grain growth during high temperature heating of FM alloy. The nucleation of DRX grains is easy to carry out at grain boundaries and defects. Grain refinement undoubtedly accelerates the nucleation process of DRX grains and promotes the degree of DRX to a certain extent. Furthermore, higher grain boundary density can also be used as a fast channel for the thermal diffusion of elements, promoting the DRX process of PM alloy [51,52].

The significant reduction in dislocation density within DDRX grains can be partially attributed to the deformation twins. As shown in Fig. 17, the deformed twins in PM alloy are observed by TEM. Some deformation twins are observed in the microstructure of PM alloy deformed at 1100 °C/0.01 s^{-1} (Fig. 17a), which are determined to be $\{10\bar{1}1\}\langle 10\bar{1}2\rangle$ compression twins (Fig. 17b). The formation of deformation twins changes the orientation of crystals and makes the new slip systems activate, which indirectly contributes to the plastic deformation. Many previous reports [53,54] revealed that the formation of deformation twins is conducive to the occurrence of dynamic softening behavior, such as the spheroidization of α phase, thereby weakening the work

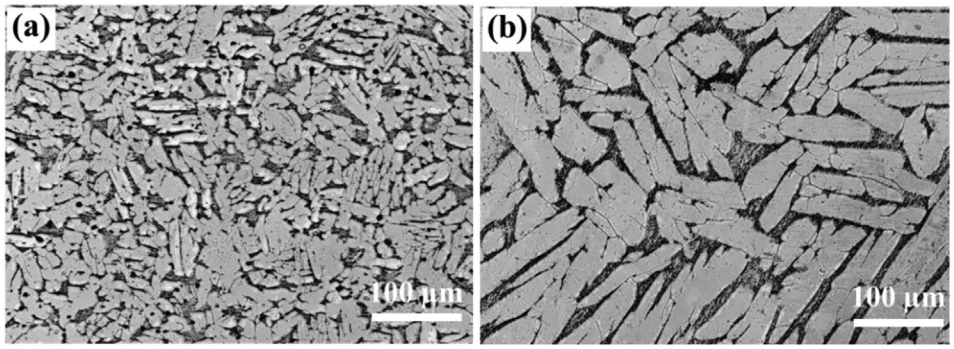

Fig. 16. OM images of the (a) PM and (b) FM alloys after heating at 1100 °C.

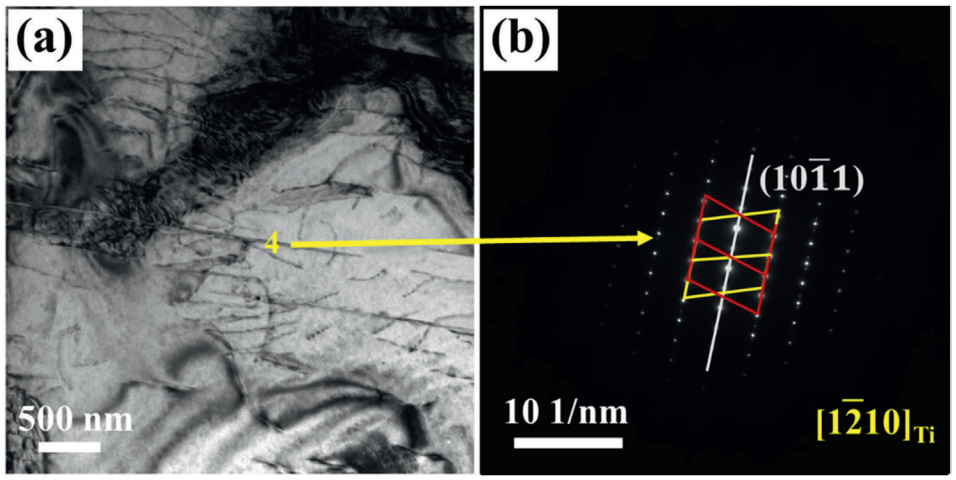

Fig. 17. TEM morphology of the PM alloy (1100 °C/0.01 s^{-1}). (a) Deformation twins; (b) SAED pattern of point 4.

hardening effect and reducing the dislocation density and deformation resistance. Therefore, the formation of deformation twins in the PM alloy is considered beneficial to its hot-working performance.

5. Conclusions

The hot working behavior and microstructure evolution of PM and FM Ti6Al4V alloys were systematically studied in this work, and the hot workability and softening mechanisms were compared. The results can be summarized as follows:

(1) The workability maps of PM and FM alloys were obtained by merging efficiency maps and instable maps. PM alloy has lower hot deformation resistance and larger area suitable for hot working at high temperature when compared with FM alloy.
(2) The formation of uneven deformation α precipitate zone and shear zone (45° angle with the matrix) are mainly occurred in the instable region of PM alloy. The coarse grains and discontinuous β phases limit the hot workability of FM alloy.
(3) PM alloy has higher DRX fraction, finer grain size, and lower dislocation density than those of FM alloy. The DRX mechanism of PM alloy is mainly DDRX, and that of FM alloy is mainly CDRX. The fine grains and the formation of deformation twins are conducive to the excellent hot working workability of PM alloy.

CRediT authorship contribution statement

Yu Pan: Writing – review & editing, Writing – original draft, Methodology, Investigation, Funding acquisition, Formal analysis, Data curation. **Xinjing Wang:** Methodology, Investigation, Formal analysis. **Guanghao Shi:** Methodology, Investigation, Formal analysis. **Jianbo Tong:** Investigation, Formal analysis, Data curation. **Jinshan Zhang:** Methodology, Investigation, Formal analysis. **Xin Lu:** Supervision, Methodology, Investigation, Funding acquisition, Formal analysis.

Declaration of competing interest

We declare that we have no known competing financial interests or personal relationships that could have appeared to influence the work reported in this paper.

Acknowledgments

This work was supported by the Science and Technology Plan Projects in Xizang Autonomous Region (No. XZ202401ZY0077), National Natural Science Foundation of China (Nos. 52571030, 52304379 and 52274359), Stable support project (No. KZ0C231524) and Shenzhen Science and Technology Innovation Commission (No. KJZD20231023100003006).

References

[1] Y. Pan, Y.C. Yang, Q.J. Zhou, X.H. Qu, P. Cao, X. Lu, Achieving synergy of strength and ductility in powder metallurgy commercially pure titanium by a unique oxygen scavenger, Acta Mater. 263 (2024) 119485.
[2] S. Zhao, R. Zhang, Q. Yu, J. Ell, R.O. Ritchie, A.M. Minor, Cryoforged nanotwinned titanium with ultrahigh strength and ductility, Science 373 (6561) (2021) 1363–1368.
[3] T.L. Zhang, Z.H. Huang, T. Yang, H.J. Kong, J.H. Luan, A.D. Wang, D. Wang, W. Kuo, Y.Z. Wang, C.T. Liu, In situ design of advanced titanium alloy with concentration modulations by additive manufacturing, Science 374 (6566) (2021) 478–482.
[4] L. Bolzoni, E.M. Ruiz-Navas, E. Gordo, Quantifying the properties of low-cost powder metallurgy titanium alloys, Mater. Sci. Eng., A 687 (2017) 47–53.
[5] J.L. Yang, G.F. Wang, X.Y. Jiao, Y. Li, Q. Liu, High-temperature deformation behavior of the extruded Ti-22Al-25Nb alloy fabricated by powder metallurgy, Mater. Char. 137 (2018) 170–179.
[6] Y. Pan, W. Li, X. Lu, M.D. Hayat, L. Yin, W. Song, X. Qu, P. Cao, Microstructure and tribological properties of titanium matrix composites reinforced with in situ synthesized TiC particles, Mater. Char. 170 (2020) 110633.
[7] B. Ya, B.W. Zhou, H.S. Yang, B.K. Huang, F. Jia, X.G. Zhang, Microstructure and mechanical properties of in situ casting TiC/Ti6Al4V composites through adding multi-walled carbon nanotubes, J. Alloys Compd. 637 (2015) 456–460.
[8] Y. Pan, J. Zhang, J. Sun, Y. Liu, C. Zhang, R. Li, F. Kuang, X. Wu, X. Lu, Enhanced strength and ductility in a powder metallurgy Ti material by the oxygen scavenger of CaB6, J. Mater. Sci. Technol. 137 (2023) 132–142.
[9] R. Xu, B. Liu, Y. Liu, Y.K. Cao, W.M. Guo, Y. Nie, S.F. Liu, High temperature deformation behavior of in-situ synthesized titanium-based composite reinforced with ultra-fine TiB whiskers, Materials 11 (10) (2018) 1863–1875.
[10] Y. Pan, J. Zhang, X. Wu, Y. Yang, F. Kuang, C. Zhang, D. Lu, X. Lu, Grain growth kinetics and densification mechanism of Ti/CaB_6 composites by powder metallurgy pressureless sintering, J. Alloys Compd. 939 (2023) 168686.
[11] X.S. Xu, H.S. Ding, W. Li, H.T. Huang, H. Liang, S. Kwak, R.R. Chen, J.J. Guo, H. Z. Fu, The smooth and notched three-point bending fatigue behavior of directionally solidified high-Nb TiAl alloy, Mater. Char. 181 (2021) 111444.
[12] Y. Pan, X. Lu, P. Cao, Microstructure evolution and mechanical properties of a novel ultrastrong and ductile PM Ti6Al4V composite, Mater. Sci. Eng., A 886 (2023) 145683.
[13] H.T. Jiang, S.W. Zeng, A.M. Zhao, X.N. Ding, P. Dong, Hot deformation behavior of β phase containing γ-TiAl alloy, Mater. Sci. Eng., A 661 (2016) 160–167.
[14] N.G. Jones, R.J. Dashwood, D. Dye, M. Jackson, The flow behavior and microstructural evolution of Ti-5Al-5Mo-5V-3Cr during subtransus isothermal forging, Metall. Mater. Trans. A 40A (2009) 1944–1954.
[15] X. Wang, L. Wang, L.S. Luo, X.D. Liu, Y.C. Tang, X.Z. Li, R.R. Chen, Y.Q. Su, J. J. Guo, H.Z. Fu, Hot deformation behavior and dynamic recrystallization of melt hydrogenated Ti6Al4V alloy, J. Alloys Compd. 728 (2017) 709–718.
[16] K. Wang, M.Y. Wu, Z.B. Yan, D.R. Li, R.L. Xin, Q. Liu, Dynamic restoration and deformation heterogeneity during hot deformation of a duplex-structure TC21 titanium alloy, Mater. Sci. Eng., A 712 (2018) 440–452.
[17] J.L. Yang, G.F. Wang, X.Y. Jiao, Y. Li, Q. Liu, High-temperature deformation behavior of the extruded Ti-22Al-25Nb alloy fabricated by powder metallurgy, Mater. Char. 137 (2018) 170–179.
[18] X.F. Bai, Y.Q. Zhao, W.D. Zeng, Z.Q. Jia, Y.S. Zhang, Characterization of hot deformation behavior of a biomedical titanium alloy TLM, Mater. Sci. Eng., A 598 (2014) 236–243.

[19] Q.Y. Zhao, F. Yang, R. Torrens, L. Bolzoni, Comparison of hot deformation behaviour and microstructural evolution for Ti-5Al-5V-5Mo-3Cr alloys prepared by powder metallurgy and ingot metallurgy approaches, Mater. Des. 169 (2019) 107682.
[20] X. Chen, B. Zhang, Y. Du, M. Liu, R. Bai, Y. Si, B. Liu, D.W. Jung, A. Osaka, Constitutive model parameter identification based on optimization method and formability analysis for Ti6Al4V alloy, Materials 15 (2022) 1748.
[21] N.K. Park, J.T. Yeom, Y.S. Na, Characterization of deformation stability in hot forging of conventional Ti-6Al-4V using processing maps, J. Mater. Process. Technol. 130–131 (2002) 540–545.
[22] Y.C. Zhu, W.D. Zeng, J.L. Liu, Y.Q. Zhao, Y.G. Zhou, H.Q. Yu, Effect of processing parameters on the hot deformation behavior of as-cast TC21 titanium alloy, Mater. Des. 33 (2012) 264–272.
[23] A. Momeni, S.M. Abbasi, Effect of hot working on flow behavior of Ti-6Al-4V alloy in single phase and two phase regions, Mater. Des. 31 (8) (2010) 3599–3604.
[24] X. Zhou, L. Fu, J. Cheng, Y. Mao, Hot deformation characteristics and processing map of Ti-25Al-14Nb-2Mo-1Fe alloy under hot working process conditions, Mater. Lett. 342 (2023) 134326.
[25] Y.F. Luo, Y.H. Xie, L. Cao, J.M. Liang, Y. Liu, D.L. Zhang, Harmonically structured Ti-6Al-4V alloy with ultrahigh strength fabricated by thermomechanical consolidation of mechanically milled TiH2/Al60V40 powder blend, Mater. Sci. Eng. 787 (2020) 139493.
[26] Y.J. Feng, J.B. Hou, L. Gao, G.R. Cui, W.C. Zhang, Research on the inhomogeneity and joint interface of in situ oriented TiBw/TA15 composites fabricated by vacuum hot-pressing sintering and canned extrusion, J. Manuf. Process. 59 (2020) 791–800.
[27] J.S. Wei, F. Yang, M. Qi, C.Z. Zhang, C.G. Chen, Z.M. Guo, Understanding processing map and microstructural evolution of powder metallurgy Ti-6Al-4V within a wide range of deformation temperatures, J. Alloys Compd. 927 (2022) 167061.
[28] S.S. Wang, C.M. Lin, R.M. Hu, G.X. Wu, W. Ali, X.G. Lu, C.H. Li, Calculation of beta transus temperature of titanium alloys by Calphad method, Rare Metal Mat. Eng. 47 (1) (2018) 181–186.
[29] N. Raja, S. Yadav, A. Kumar, G. Gautam, Hot working and microstructural response of ultrasonically fabricated 2 wt%ZrB_2/AA7068 composite, J. Alloys Compd. 965 (2023) 171412.
[30] L. Qiao, R.V. Ramanujan, J.C. Zhu, Optimized hot working parameters of Fe2.5Ni2.5CrAl multi-principal element alloys, J. Alloys Compd. 925 (2022) 166594.
[31] K.T. Son, M.H. Kim, S.W. Kim, J.W. Lee, S.K. Hyun, Evaluation of hot deformation characteristics in modified AA5052 using processing map and activation energy map under deformation heating, J. Alloys Compd. 740 (2018) 96–108.
[32] J.K. Fan, H.C. Kou, M.J. Lai, B. Tang, H. Chang, J.S. Li, Characterization of hot deformation behavior of a new near beta titanium alloy: Ti-7333, Mater. Des. 49 (2013) 945–952.
[33] M. Kai, Z. Horita, T.G. Langdon, Developing grain refinement and superplasticity in a magnesium alloy processed by high-pressure torsion, Mater. Sci. Eng. 488 (1) (2008) 117–124.
[34] Y.V.R.K. Prasad, Processing maps: a status report, J. Mater. Eng. Perform. 12 (2003) 638–645.
[35] K. Yang, H.F. Lou, Z.T. Peng, M.X. Guo, H. Wang, Y.D. Mo, F. Liu, Y.P. Wang, M. M. Wang, W. Zhou, D. Liang, Hot strain induced dynamic recrystallization, precipitation and coordinated deformation behaviors of Cu-4.3 wt%Ti alloy, J. Alloys Compd. 1022 (2025) 179938.
[36] Y.V.R.K. Prasad, T. Seshacharyulu, Processing maps for hot working of titanium alloys, Mater. Sci. Eng. 243 (1998) 82–88.
[37] X.J. Lin, H.J. Huang, X.G. Yuan, Y.X. Wang, B.W. Zheng, X.J. Zuo, G. Zhou, Establishment and validity verification of the hot processing map of a Ti-47.5Al-2.5V-1.0Cr-0.2Zr alloy with a lamellar microstructure, Mater. Char. 183 (2022) 111599.
[38] M.T. Jia, J.M. Liang, D.L. Zhang, C. Kong, B. Gabbitas, Effects of holding time during pre-sintering and post-forging annealing on the microstructure and mechanical properties of Ti parts fabricated by powder compact forging, Mater. Sci. Eng.A 655 (2016) 113–121.
[39] M. Jia, Y. Alshammari, F. Yang, L. Bolzoni, Effect of heat treatment on the microstructure and mechanical properties of blended elemental Ti-6Al-4V produced by powder forging, Mater. Sci. Eng.A 791 (2020) 139724.
[40] Y.V.R.K. Prasad, H.L. Gegel, S.M. Doraivelu, J.C. Malas, J.T. Morgan, K.A. Lark, D. R. Barker, Modeling of dynamic material behavior in hot deformation: forging of Ti-6242, Metall. Trans. A 15 (1984) 1883–1892.
[41] Y.f. Zheng, S.L. Xiao, Z.Q. Liang, S.W. Han, J.H. Yang, L.J. Xu, X. Xue, J. Tian, Influence of thermal exposure on compressive creep behavior and dynamic recrystallization of (TiB+TiC+Y_2O_3)/α-Ti composite, Mater. Sci. Eng. 908 (2024) 146957.
[42] X.L. Liang, Z.Q. Liu, B. Wang, Dynamic recrystallization characterization in Ti-6Al-4V machined surface layer with process-microstructure-property correlations, Appl. Surf. Sci. 530 (2020) 147184.
[43] Q. Liu, L.M. Fang, Z.W. Xiong, J. Yang, Y. Tan, Y. Liu, Y.J. Zhang, Q. Tan, C.C. Hao, L.H. Cao, J. Li, Z.P. Gao, The response of dislocations, low angle grain boundaries and high angle grain boundaries at high strain rates, Mater. Sci. Eng. 822 (2021) 141704.
[44] X.F. Chen, B. Tang, D. Liu, B.B. Wei, L. Zhu, R.C. Liu, H.C. Kou, J.S. Li, Dynamic recrystallization and hot processing map of Ti-48Al-2Cr-2Nb alloy during the hot deformation, Mater. Charact. 179 (2021) 111332.
[45] D.G. Cram, H.S. Zurob, Y.J.M. Brechet, C.R. Hutchinson, Modelling discontinuous dynamic recrystallization using a physically based model for nucleation, Acta Mater. 57 (17) (2009) 5218–5228.
[46] Y.X. Wang, G.Q. Zhao, X. Xu, X.X. Chen, C.S. Zhang, Constitutive modeling, processing map establishment and microstructure analysis of spray deposited Al-Cu-Li alloy 2195, J. Alloys Compd. 779 (2019) 735–751.
[47] Z.C. Sun, H.L. Wu, J. Cao, Z.K. Yin, Modeling of continuous dynamic recrystallization of Al-Zn-Cu-Mg alloy during hot deformation based on the internal-state-variable (ISV) method, Int. J. Plast. 106 (2018) 73–87.
[48] S. Wang, J.R. Luo, L.G. Hou, J.S. Zhang, L.Z. Zhuang, Physically based constitutive analysis and microstructural evolution of AA7050 aluminum alloy during hot compression, Mater. Des. 107 (2016) 277–289.
[49] X. Wang, L. Wang, L.S. Luo, H. Yan, X.Z. Li, R.R. Chen, Y.Q. Su, J.J. Guo, H.Z. Fu, High temperature deformation behavior of melt hydrogenated (TiB + TiC)/Ti6Al4V composites, Mater. Des. 121 (2017) 335–344.
[50] S.Z. Zhang, J.W. Liu, Q.Y. Zhao, C.J. Zhang, L. Bolzoni, F. Yang, Microstructure characterization of a high strength Ti6Al4V alloy prepared from a powder mixture of TiH_2 and 60Al40V masteralloy powders, J. Alloys Compd. 818 (2020) 152815.
[51] H. Iwaoka, M. Arita, Z. Horita, Hydrogen diffusion in ultrafine-grained palladium: roles of dislocations and grain boundaries, Acta Mater. 107 (2016) 168–177.
[52] M.S. Hooshmand, C. Niu, D.R. Trinkle, M. Ghazisaeidi, First-principles prediction of oxygen diffusivity near the (1012) twin boundary in titanium, Acta Mater. 156 (2018) 11–19.
[53] Y. Chong, T. Bhattacharjee, R. Gholizadeh, J. Yi, N. Tsuji, Investigation on the hot deformation behaviors and globularization mechanisms of lamellar Ti6Al4V alloy within a wide range of deformation temperatures, Materialia 8 (2019) 100480.
[54] P. Wang, X.P. Tan, M.L.S. Nai, J. Wu, J. Wei, Deformation induced nanoscale twinning improves strength and ductility in additively manufactured titanium alloys, Mater. Sci. Eng. 833 (2022) 142568.